Epitaxial Growth of Monolayer MoS_2 on $SrTiO_3$ Single Crystal Substrates for Applications in Nanoelectronics

Peiyu Chen,[†,*] *Wenshuo Xu,*[†] *Yakun Gao, Jamie H. Warner, Martin R. Castell**

Department of Materials, University of Oxford, Parks Road, Oxford, OX1 3PH, United Kingdom

ABSTRACT: Monolayer molybdenum disulfide (MoS_2) crystals grown on amorphous substrates such as SiO_2 are randomly oriented. However, when MoS_2 is grown on crystalline substrates, the crystal shapes and orientations are also influenced by their epitaxial interaction with the substrate. In this paper we present the results from chemical vapor deposition growth of MoS_2 on three different terminations of single crystal strontium titanate ($SrTiO_3$) substrates. On $SrTiO_3(111)$ the monolayer MoS_2 crystals form equilateral triangles with two main orientations, in which they align their $<2\bar{1}\bar{1}0>$-type directions (i.e., the sulfur-terminated edge directions) with the $<1\bar{1}0>$-type directions on $SrTiO_3$. This arrangement allows near perfect coincidence epitaxy between seven MoS_2 unit cells and four $SrTiO_3$ unit cells. On $SrTiO_3(110)$ the MoS_2 crystals tend to align their edges with both $<1\bar{1}0>$ and $<1\bar{1}\bar{2}>$ directions on $SrTiO_3$ as these both provide favorable coincidence lattice registry. This distorts the crystal shapes and introduces an additional strain detectable by photoluminescence. When triangular MoS_2 crystals are grown on $SrTiO_3(001)$, they again show a preference to align their edges with the $<1\bar{1}0>$ directions on $SrTiO_3$. Our observations can be explained if the interfacial van der Waals (vdW) bonding between MoS_2 monolayers and $SrTiO_3$ is greatest when the maximum commensuration between the lattices is achieved. Therefore, a key finding of this paper is that the vdW interaction between MoS_2 and $SrTiO_3$ substrates determines the supported crystal shapes and orientations by the epitaxial relations. Controlled crystal orientations make the growth of large sheets of MoS_2 possible when there are multiple nucleation sites. This minimizes the number of grain boundaries and optimizes electronic properties of the material, e.g., charge mobility, which is crucial for the application of monolayer MoS_2 in next-generation nanoelectronic devices.

KEYWORDS: *MoS_2, $SrTiO_3$, van der Waals epitaxy, scanning tunneling microscopy, chemical vapor deposition, Raman spectroscopy, photoluminescence spectroscopy, 2D materials*

1. INTRODUCTION

Monolayer MoS_2 has been extensively studied as the prototypical material of the family of transition metal dichalcogenides (TMDCs).[1] It was discovered that the electronic properties of TMDCs are drastically affected by dimensionality: MoS_2 in its bulk form is a semiconductor with an indirect bandgap of 1.2–1.3 eV, which transforms into a direct bandgap of 1.8–1.9 eV when the material is as thin as a monolayer.[2,3] These bandgap energies span the visible and near-infrared range of the electromagnetic spectrum, and therefore MoS_2 is a promising candidate for optoelectronic applications.[4] Monolayer MoS_2 is also viewed as a two-dimensional (2D) semiconductor with great potential because of its high charge mobility of more than 200 $cm^2\ V^{-1}\ s^{-1}$ and an on/off current ratio up to $\sim 10^8$.[5] These properties make it competitive with graphene for use in novel low-power digital electronics.[5]

For a 2D material like MoS_2, the growth technique of chemical vapor deposition (CVD) has the advantage over exfoliation that it allows the substrate to influence the chemistry and properties of the MoS_2 monolayers. This is important from a technological point of view because the properties of a 2D material can be highly sensitive to its interfaces.[1] CVD growth on a well-prepared substrate results in a collection of large MoS_2 domains that have controllable morphology.[6,7] In particular, epitaxy has been shown to effectively control MoS_2 crystal orientations, which is required to minimize the concentration of grain boundaries in the MoS_2 layer.[7,8] This is especially important in large-area synthesis of MoS_2 because grain boundaries are detrimental to the electrical properties (e.g., charge mobility) of polycrystalline films.[9–11] By its nature, epitaxial growth cannot occur on amorphous substrates like SiO_2.[12] On crystalline substrates, the main mechanism that allows epitaxy to occur is generally believed to be due to van der Waals (vdW) forces for both metallic and non-metallic substrates,[7,8,13–15] e.g., *c*-plane sapphire[7,8] and Au(111).[15] Although the vdW interaction is relatively weak when compared to in-plane covalent bonding, it still provides a significant force between two 2D sheets. It has been confirmed to powerfully control the interlayer epitaxy of MoS_2 bilayers, where the AA and AB stacking configurations (0° and 60° relative layer rotation) are overwhelmingly favored compared to others.[16] Furthermore, the indirect-to-direct transition of the MoS_2 bandgap in the monolayer limit is a direct consequence of the absence of neighboring layers, which only interact via vdW forces. This means that the interlayer forces perturb each other's electronic band structures. Therefore, the importance of vdW bonding should not be overlooked with respect to interfacial bonding between MoS_2 and its substrate. Nevertheless, other possible interfacial bonding mechanisms have also been reported, including electrostatic attraction between MoS_2 and sapphire[7] and chemical bonding between S and various metals.[17–20] The nature of the Au-S bond is particularly controversial; it is claimed to perturb the electronic structure very little in some studies[15,18] and have a covalent nature in others.[17]

Finding suitable substrate materials is an important step towards epitaxy or orientation control in the synthesis of MoS_2 films. The substrates used in our work are electrically conducting Nb-doped (0.5 wt%) $SrTiO_3$ crystals. $SrTiO_3$ has attracted substantial interest since the 1970s owing mostly to its versatile crystal surfaces.[21] It was chosen for our study because several surface terminations with different symmetries can be readily prepared. MoS_2 was grown on the three well-studied $SrTiO_3$ terminations, (111), (110), and (001). The crystallinity of $SrTiO_3$ encourages MoS_2 monolayer crystals to grow epitaxially, and the different symmetries of the three terminations lead to distinct epitaxial behavior. Overall, the interaction between MoS_2 and $SrTiO_3$ is found to influence the orientations, shapes, and optical properties of MoS_2 monolayers.

The ability to regulate these properties of monolayer MoS_2 is important in the synthesis of large-scale layers of the material with minimal grain boundaries and controlled bandgaps. This will improve the potential of monolayer MoS_2 in its application to nanoelectronics and optoelectronics.

2. EXPERIMENTAL SECTION

2.1. Preparation of Substrates. $SrTiO_3$ single crystals (7 × 2 × 0.5 mm^3) doped with Nb at 0.5% by weight were supplied by PI-KEM, U.K, with epi-polished (111), (110), and (001) surfaces. $SrTiO_3$ is an insulator with a band gap of 3.2 eV at 25 °C.[22] The Nb dopant was included to generate sufficient electrical conductivity at room temperature for scanning tunneling microscopy (STM) imaging. The preparation and imaging of $SrTiO_3$ surfaces were carried out in an ultra-high vacuum (UHV) STM, which is a custom-built JEOL JSTM 4500s model (base pressure 10^{-8} Pa). $SrTiO_3$ surfaces were prepared to terminate with previously well-characterized reconstructions, requiring different Ar^+ ion sputtering conditions, annealing temperatures, durations, and O_2 partial pressures.[23–25]

2.2. CVD Growth and Transfer of MoS_2. Molybdenum trioxide (MoO_3, powder, ≥99.5%, Sigma-Aldrich) and sulfur (S, powder, ≥99.5%, Sigma-Aldrich) were used to synthesize MoS_2 monolayers on $SrTiO_3$ using the atmospheric pressure CVD method. A schematic diagram of the CVD setup is shown in Figure 1c. $SrTiO_3$ substrates were placed face-up and downstream with respect to the precursors, which were 20 mg MoO_3 and 300 mg S, loaded into two tubes with 12 mm and 22 mm diameters, respectively. The system was first flushed with 500 sccm argon to drive off oxygen. Subsequently, S vapor was pre-introduced at 190 °C for 15 min with a decreased argon flow rate of 150 sccm, which ensured that the system was sulfur rich so that the as-grown MoS_2 crystals were triangles with S edge terminations. Then the MoO_3 precursor and the $SrTiO_3$ substrate were heated to 300 °C and 782 °C, respectively. The reaction lasted 30 min with 100 sccm argon carrier gas and finished with a fast cooling process.

MoS_2 monolayers grown on a SiO_2/Si substrate were first spin-coated with a thin film of poly(methyl methacrylate) (PMMA, 8 wt% in anisole, 495k molecular weight) at 4500 rpm for 60 s, followed by a 90 s curing process at 180 °C. The SiO_2 layer was etched off by floating the samples on a 1 M potassium hydroxide (KOH, Sigma-Aldrich) aqueous solution at room temperature, whereby the planar strain in the MoS_2 monolayer was released. The isolated film of PMMA/MoS_2 was then rinsed in deionized (DI) water three times for 1 h each time. Following this, a pre-cleaned $SrTiO_3$ substrate was submerged into the DI water to support the film. The as-transferred sample was dried overnight in a ventilation environment, after which it was baked at 150 °C for 20 min to enhance the MoS_2–substrate adhesion. The PMMA coating was removed by soaking the sample in a 55 °C acetone bath for 6 h. Finally, to remove the trapped contaminants for a cleaner interface, the sample was annealed at 200 °C for 1 h with 150 sccm Ar as the carrier gas.

2.3. Characterization. The MoS_2 crystals were imaged by scanning electron microscopy (SEM) and STM. SEM was performed using a Zeiss Merlin and a Hitachi-4300, both at an accelerating voltage of 3 kV. STM images were processed by Smart Align,[27,28] Gwyddion, and WSxM.[29] Raman spectroscopy and photoluminescence (PL) were conducted using a JY Horiba LabRAM ARAMIS imaging confocal Raman microscope with a 532 nm excitation wavelength and 12.5 mW laser power. The laser spot size was ~1 μm, and the acquisition times were 35 s for Raman and 5 s for PL spectra.

3. RESULTS

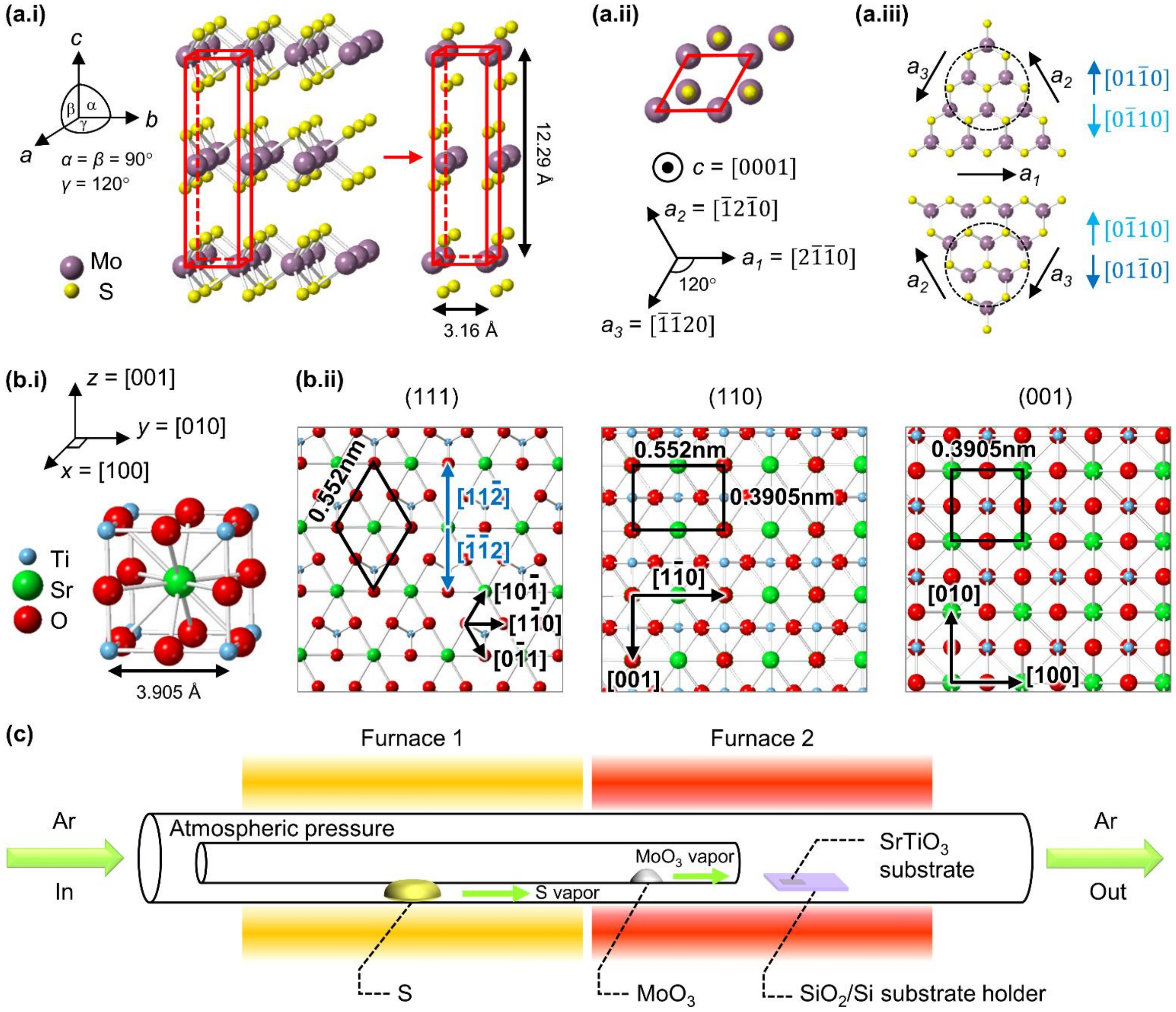

Figure 1. Crystal structures of MoS_2 and $SrTiO_3$ and the CVD system. (a.i) Bulk MoS_2 with a red rhombic prismatic unit cell. (a.ii) Top view of MoS_2 with the crystallography defined by the four-index notation. (a.iii) Top view of monolayer triangular crystals of MoS_2. (b.i) Unit cell of $SrTiO_3$. (b.ii) Atomic top view of bulk-terminated $SrTiO_3$(111), (110), and (001) planes with unit cells and lattice directions labelled. In (111), only two layers of atoms are shown for clarity. (c) CVD setup for the synthesis of MoS_2 crystals.

Prior to presenting our experimental results, it is helpful to unambiguously define the crystallography of both MoS_2 and $SrTiO_3$ for the purpose of epitaxial analysis. Figure 1a.i is the side view of the 3D structure of 2H-MoS_2, the thermodynamically stable polytype of MoS_2.[30] Two other common polytypes are called 1T- and 3R-MoS_2, but they are not discussed here. The 2H-MoS_2 crystal consists of covalently bonded S-Mo-S sandwich layers held together by vdW forces.[2,3,30] The unit cell is labelled in red, and a single unit cell of the lattice is shown to the right of the red arrow. It is a hexagonal structure with lattice parameters of $a = b = 3.1602$ Å, $c = 12.294$ Å and angles of $\alpha = \beta = 90°$, $\gamma = 120°$; the space group is $P6_3/mmc$ (194).[30] Figure 1a.ii is the top view of MoS_2. In common with other hexagonal systems, it is useful to employ a four-index notation to emphasize the equivalence between crystallographically-equivalent directions.[31] For example, the a_1, a_2 and a_3 directions in Figure 1a.ii are all of the $<2\bar{1}\bar{1}0>$ type,[31,32] which highlights the symmetry of the structure. Many studies term the basal plane of MoS_2 as (0001),[15,33] implying the use of the four-index notation, though the in-plane crystallography tends not to be discussed. Figure 1a.iii shows the top view of triangular MoS_2 monolayers, which are 60° (or 180°) rotated with respect to each other. Their S-terminated edges are aligned along the $<2\bar{1}\bar{1}0>$-type directions. It should be noted that the orientations of the two crystals are not equivalent. For example, in the dashed circles the two structures have the same skeleton of S atoms, but the Mo atoms are located differently. In other words, if the bottom layer of S atoms choose to orient in a specific way on the substrate, it can result in two different overall configurations due to the Mo atoms. For convenient subsequent analysis, it is useful to define the upward and downward crystallographic directions, which are $[01\bar{1}0]$ and $[0\bar{1}10]$, and they are inequivalent. Note that these directions are equivalent in a bulk MoS_2 crystal, which has in-plane hexagonal symmetry, which is reduced to three-fold symmetry in a monolayer.

$SrTiO_3$ adopts a perovskite structure with a cubic lattice above 105 K (a = 3.905 Å),[23] and its unit cell is shown in Figure 1b.i. The Ti^{4+} ions are octahedrally coordinated with respect to the O^{2-} ions, and the Sr^{2+} ions are in a site that is 12-fold coordinated by O^{2-} ions. The three surface terminations of interest in our study are presented in Figure 1b.ii. The (111) termination is a three-fold symmetric surface with a rhombic unit cell drawn in black. On close inspection of the unit cell, it can be seen that the upper and lower halves are not equivalent, as there is an additional Ti atom in the lower half, one atomic layer down from the topmost Sr and O atoms. The Ti layer reduces the symmetry of the topmost layer from six-fold to three-fold. Again, it is helpful to define the upward and downward crystallographic directions on $SrTiO_3$(111), $[11\bar{2}]$ and $[\bar{1}\bar{1}2]$, a pair of inequivalent directions. Next, the (110) surface of $SrTiO_3$ has two-fold symmetry and the unit cell is a rectangle (Figure 1b.ii). Finally, $SrTiO_3$(001) has four-fold symmetry with a square surface unit cell (Figure 1b.ii).

Although the as-supplied $SrTiO_3$ samples used in this work were epi-polished on the top surface by the manufacturer to a mirror finish, a small depth of disordered polishing damage will remain. Therefore, in order to ensure that the crystallinity of the sample extends to the top atomic surface layer, we processed all our samples through UHV annealing and/or Ar^+ ion sputtering. This preparation process eliminates the polishing damage and allows the surface to become crystalline, atomically flat, and relatively free of contaminants. The surface reconstructions we observe following UHV annealing cannot survive in an ambient environment. Therefore the interface between the MoS_2 crystals and the $SrTiO_3$ substrates will differ from the UHV-prepared samples, but with our procedure we ensured that the maximum degree of substrate crystallinity was created prior to CVD growth.

A schematic diagram of the CVD system is shown in Figure 1c. The MoO_3 and S precursors were loaded in two quartz tubes in two separate furnaces for independent control of their temperatures. The $SrTiO_3$ substrate was supported on a larger SiO_2/Si wafer acting as a holder. The precursor vapors were transported by Ar flow under atmospheric pressure downstream onto the substrate surface to grow MoS_2.

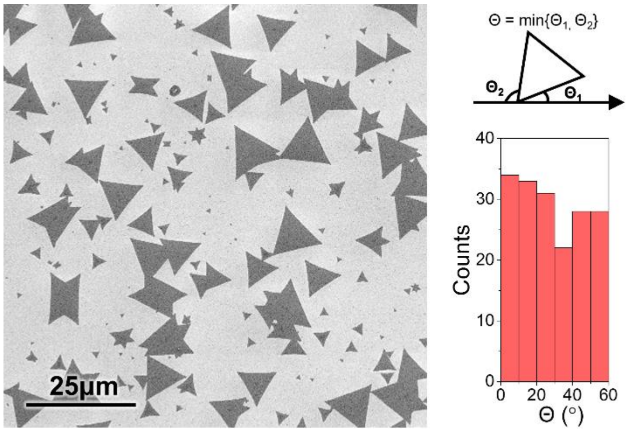

Figure 2. SEM image of monolayer MoS_2 crystals on SiO_2/Si and the orientation histogram of the MoS_2 crystals, measured according to the standard in the top right part of the figure.

For purposes of comparison, we first present data from an amorphous substrate. Figure 2 is an SEM image of MoS_2 crystals grown on SiO_2/Si. As one would expect from sulfur-rich growth conditions, the MoS_2 monolayers preferentially adopt triangular geometries.[12] The orientation of any crystal was measured as the angle it makes with the horizontal line below it, whichever side is smaller (Figure 2 top right). Their orientations are randomly distributed, as shown in the histogram in the right-hand panel. The random distribution demonstrates that the vdW interaction between the amorphous substrate and the MoS_2 monolayers induces no orientation preferences for the crystal growth.

3.1. MoS_2 on $SrTiO_3(111)$.

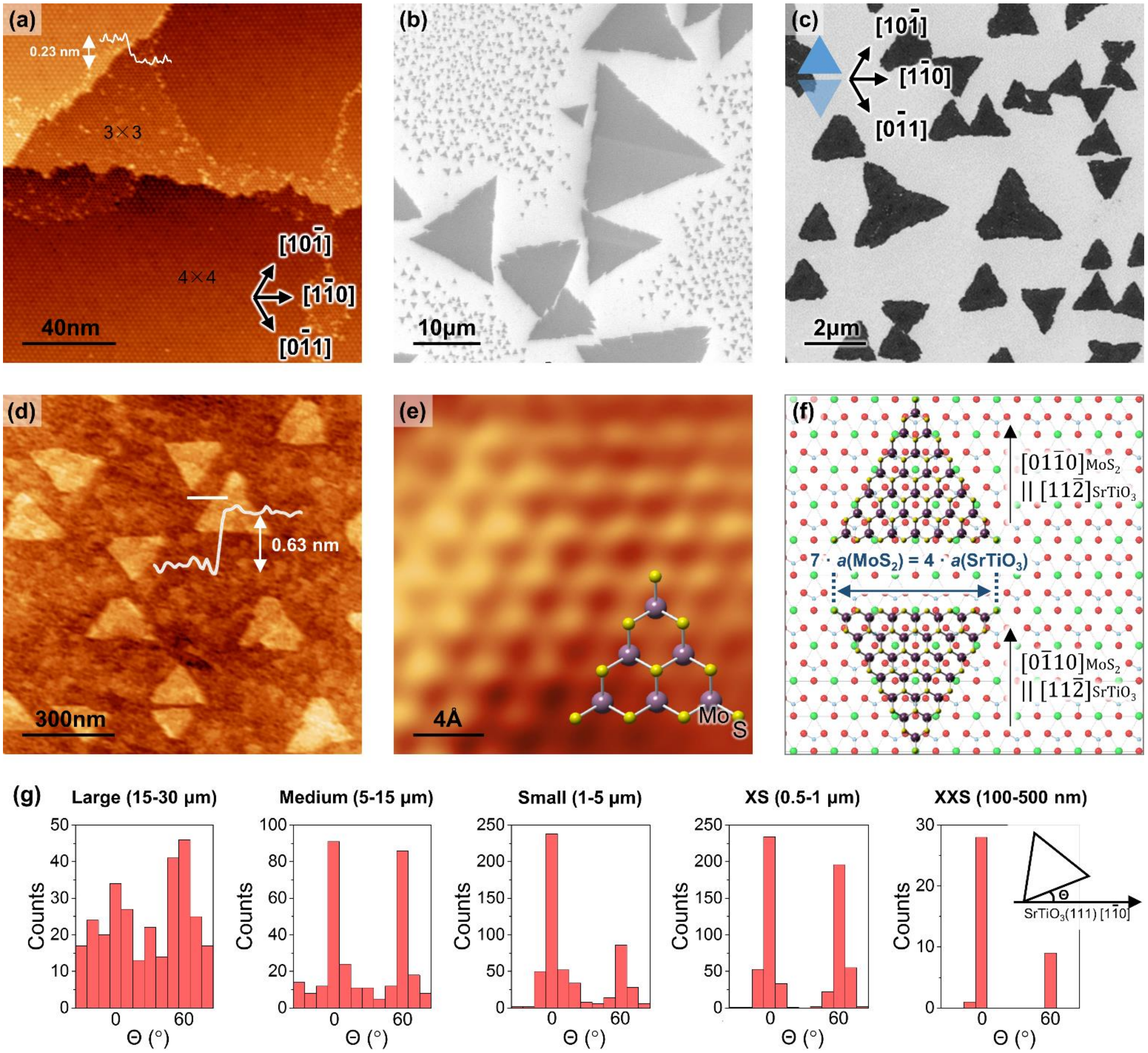

Figure 3. Models and images of $SrTiO_3(111)$ and MoS_2 on $SrTiO_3(111)$. (a) STM image of reconstructed $SrTiO_3(111)$, showing terraces with (3 × 3) and (4 × 4) reconstructed domains. Two example domains are labelled. Each step height is 0.23 ± 0.03 nm and corresponds to the d_{111} lattice spacing (V_s = 2.0 V, I_t = 0.38 nA). (b) SEM image showing MoS_2 crystals with a large range of sizes (laterally 0.5–30 μm). (c) SEM image of small crystals (1–

3 μm). The preferred crystal orientations are drawn as schematics, where the darker blue triangle is more strongly preferred. (d) STM image showing very small MoS_2 crystals (200–400 nm), with a line profile showing monolayer thickness ($V_s = 1.5$ V, $I_t = 0.09$ nA). (e) Atomically resolved STM image of a MoS_2 monolayer showing a triangular atomic lattice with a periodicity of 3.16 ± 0.09 Å, corresponding to the in-plane S-S distance ($V_s = 1.1$ V, $I_t = 0.14$ nA). An atomic model of monolayer MoS_2 is superimposed assuming that S atoms are imaged by the STM. (f) Atomic models showing the two preferred orientations of MoS_2 crystals on $SrTiO_3(111)$. The interface crystallography is written next to each orientation. Also, 7 MoS_2 unit cell lengths (S-S spacings) = 4 $SrTiO_3<1\bar{1}0>$ unit lengths (Sr-Sr spacings). The substrate lattice directions in (a) also apply to panels (b–f). (g) Orientation histograms for MoS_2 crystals of different sizes, measured according to the standard on the far right.

Figure 3a is an STM image of the $SrTiO_3(111)$ surface composed of domains of (3 × 3) and (4 × 4) reconstructions,[23,34] with the average terrace step height being measured as 0.23 ± 0.03 nm (d_{111} lattice spacing = 0.225 nm). This surface is generated by Ar^+ ion sputtering at 500 eV for 8 minutes, and subsequently annealing at 1140 °C for 3 hours in 4.5×10^{-4} Pa O_2. It demonstrates that the outermost surface of our substrate is crystalline. Note that the white dots in Figure 3a may be contaminants or regions that are not well reconstructed, which cannot be completely avoided even by careful UHV treatment. They exist in the best STM images of $SrTiO_3$ surfaces reported.[23–25] In previous epitaxial studies of MoS_2 on crystalline substrates, e.g., *c*-plane sapphire,[7,8] as-received / epi-polished substrates were used. These substrates contain polishing damage and contaminants that are orders of magnitude greater than UHV-treated samples, but epitaxy was still found and studied.

Figure 3b shows a typical SEM image of MoS_2 crystals on $SrTiO_3(111)$. The larger crystals (those with lateral sizes over 5 μm) with sulfur-terminated edges[12,35,36] appear to be randomly oriented, but in the close-up image of smaller crystals (Figure 3c), the crystals show more regular alignment. The lattice directions of the $SrTiO_3(111)$ substrate are also drawn at the top-left corner for reference: one can see that the small triangles mostly have their three sides parallel to the three $<1\bar{1}0>$-type directions on $SrTiO_3(111)$, resulting in two main orientations as represented by the two blue schematic triangles. Another observation is that one of the two preferred orientations is more abundant (the darker blue triangle pointing up). Even smaller crystals were examined by STM, as shown in Figure 3d. This figure also shows that STM images show the height of the MoS_2 monolayers to be 0.63 ± 0.06 nm. This agrees with the previously reported value of 0.65 nm.[5,37] An atomically-resolved STM image in Figure 3e shows a triangular pattern of bright dots with a periodicity of 3.16 ± 0.09 Å, which agrees with the literature value of 3.16 Å.[30] Because monolayer MoS_2 terminates with an outer plane of S atoms, from the topographical point of view the bright protrusions in STM images are generally thought to be S atoms.[38,39]

The observations regarding epitaxy were statistically visualized by orientation histograms and are shown in Figure 3g. Note that in the SEM images (Figure 3b,c) some triangles have zig-zag or concave edges which are sulfur-terminated as the MoS_2 crystals were grown in a sulfur-rich environment.[12] When an edge is not completely flat, its direction is measured as that of the straight line connecting its two ends, which is a good estimate of the sulfur-termination direction.[12] The MoS_2 crystals were grouped into large (15–30 μm), medium (5–15 μm), small (1–5 μm), XS (0.5–1 μm), and XXS (100–500 nm), according to their lateral sizes. In all cases, the two highest peaks are at 0° and 60°, indicating the two dominant orientations of MoS_2 crystals: ‘$(0001)_{MoS_2} \parallel (111)_{SrTiO_3}$, $[01\bar{1}0]_{MoS_2} \parallel [11\bar{2}]_{SrTiO_3}$’ and ‘$(0001)_{MoS_2} \parallel (111)_{SrTiO_3}$, $[0\bar{1}10]_{MoS_2} \parallel [11\bar{2}]_{SrTiO_3}$’.

In the preferred orientations, MoS_2 and $SrTiO_3(111)$ are both symmetry coincident and lattice commensurate: the length of 7 MoS_2 unit cells (7 × 0.316 nm = 2.212 nm) equals the length of 4 $SrTiO_3$ unit cells (4 × 0.552 nm = 2.208 nm) with a small difference of < 0.2%, as illustrated in Figure 3f. In the histograms in Figure 3g, the preferred angular orientations are better defined for smaller crystals, and this can be explained by kinetics. The large crystals undergo a rapid growth process with only little time to optimize their orientations relative to the substrate. However, the smaller crystals grow slowly and are able to rotate into orientations that optimize the vdW interaction with the substrate. Another interesting possibility is that the smaller MoS_2 islands are constrained by the lattice commensuration so that they cannot grow to larger sizes. If so, the crystals would have grown rapidly to a certain size, beyond which it is difficult to expand further due to the lattice constraints. In this case we should observe a disproportionately large number of crystals at that size. However, such an uneven size distribution is not seen.

It is likely that one of the two preferred orientations is the thermodynamically more stable. Particularly in the histograms for small and XXS crystals, there is a statistically significant difference between the heights of the two peaks. In Figure 3f are the atomic models of the two preferred orientations, in which the MoS_2 crystals sit in the same way as those in Figure 1a.iii. We illustrated in Figure 1a.iii and b.ii that on both monolayer MoS_2 and $SrTiO_3(111)$, the crystallographic directions pointing up and down are distinct. Hence, the two orientations of MoS_2 crystals on $SrTiO_3(111)$ shown in Figure 3f are physically distinct, and their respective interface crystallography is labelled next to them. We conclude that one of the two orientations is favored, but they are not distinguishable from our results.

3.2. MoS_2 on $SrTiO_3$(110).

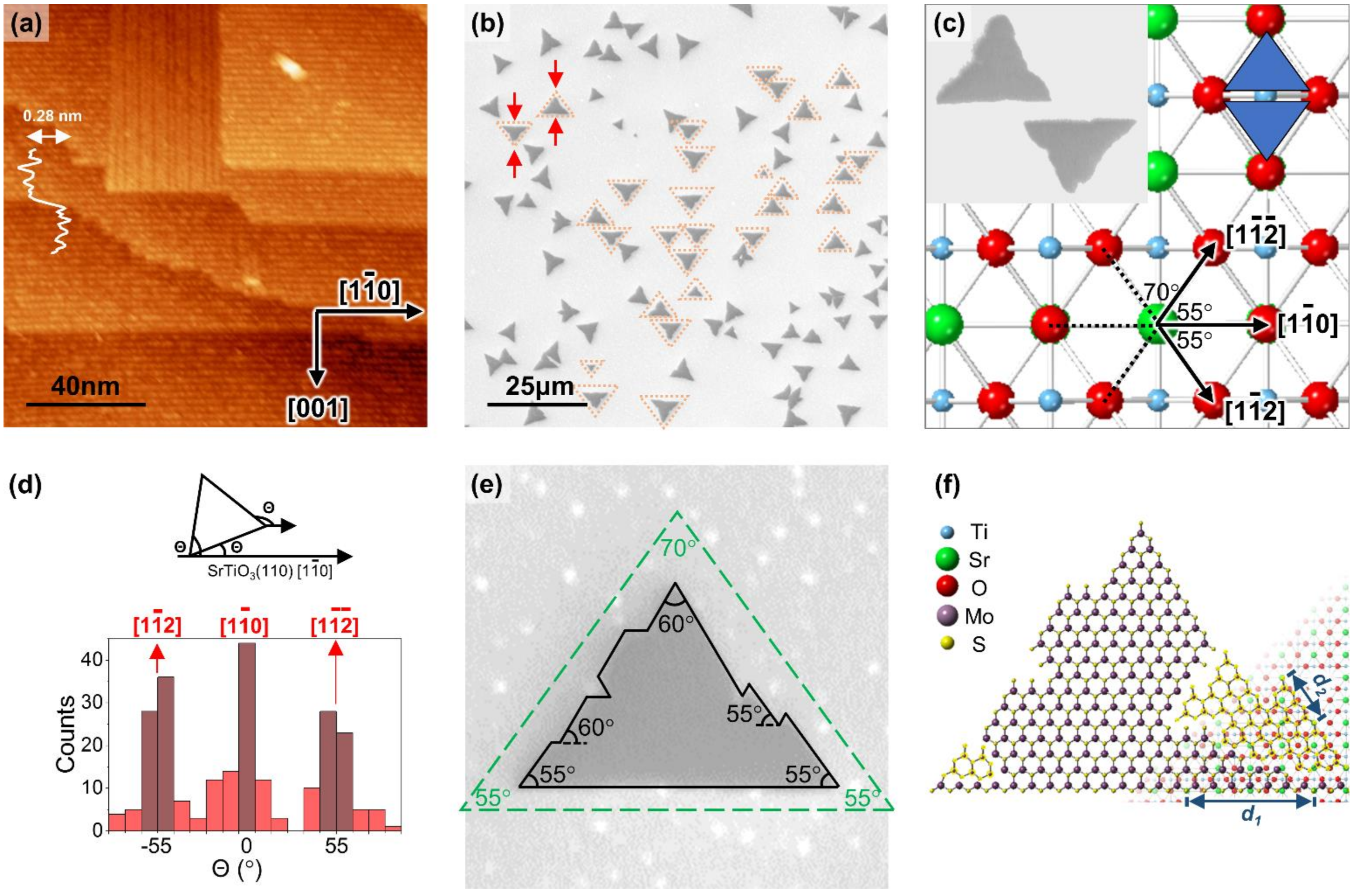

Figure 4. Models and images of $SrTiO_3$(110) and MoS_2 on $SrTiO_3$(110). (a) STM image of $SrTiO_3$(110) showing terraces mainly made of the (6 × 1) reconstruction. Each step height is 0.28 ± 0.04 nm, corresponding to the d_{110} lattice spacing (V_s = 1.0 V, I_t = 0.40 nA). (b) SEM image of MoS_2 on $SrTiO_3$(110). Some crystal shapes are 'compressed' along the [001] direction compared to equilateral triangles (outlined by orange dashed lines and red arrows at the top left). (c) Blue schematic triangles on the atomic model of $SrTiO_3$(110) representing the most commonly observed crystal orientations of MoS_2. The inset is an SEM image of MoS_2 crystals with the preferred

orientations. (d) Edge orientation histogram of MoS_2 crystals on $SrTiO_3$(110), measured according to the standard above. (e) SEM image of a typically-shaped MoS_2 crystal, with its rough edges highlighted in black. (f) Atomic model of a MoS_2 crystal on $SrTiO_3$(110), with the same shape in panel (e). The rotated lattice parts are highlighted in yellow. 'd_1' = 7 MoS_2 unit cell lengths (S-S spacings) = 4 $SrTiO_3[1\bar{1}0]$ unit lengths (Sr-Sr spacings). 'd_2' = 3 MoS_2 unit cell lengths (S-S spacings) = 1 $SrTiO_3[1\bar{1}2]$ unit length (Sr-Sr spacing). The substrate lattice directions in (a) also apply to panels (b,c,e,f).

The $SrTiO_3$(110) substrates are treated in UHV to create a well-defined crystalline top surface. An STM image of the terraces is presented in Figure 4a, produced by an anneal at 890 °C for 2 hours, followed by another anneal at 910 °C for 3 hours, both in UHV. It mainly consists of the (6 × 1) reconstruction.[24,40,41]

Figure 4b is a typical SEM image of MoS_2 on $SrTiO_3$(110), from which it is noticeable that some triangles appear to be vertically distorted compared to the shape of equilateral triangles. This is illustrated on two of them by the red arrows at the top left of the image. There are two most commonly observed orientations, which are shown in the SEM image in Figure 4c and also drawn as blue schematic triangles on the atomic model of the substrate. When compared with the substrate lattice, they each have their three sides parallel to $[1\bar{1}0]$, $[1\bar{1}\bar{2}]$, and $[1\bar{1}2]$ of the $SrTiO_3$(110) substrate. In this case the direction of each crystal edge was measured according to the standard in Figure 4d. In the resulting histogram, the brown peaks correspond to the three directions identified above, as expected. For example, $[1\bar{1}\bar{2}]$ is at 55° anticlockwise relative to $[1\bar{1}0]$, which is also shown in Figure 4c. If we refer to Figure 4c, we can see that such triangles with their edges parallel to $[1\bar{1}0]$, $[1\bar{1}\bar{2}]$, and $[1\bar{1}2]$ have three internal angles of 70°, 55°, and 55°.

The $[1\bar{1}0]$ direction is favored because of the 7:4 coincidence epitaxy, similar to the case on $SrTiO_3(111)$. However, on $SrTiO_3(110)$ only one edge of any MoS_2 triangle can align with such a direction. Nevertheless, among those low-index (i.e., relatively close-packed) lattice directions which are at ~60° to $<1\bar{1}0>$, the $<1\bar{1}\bar{2}>$ directions are favored for two reasons. The first one is again lattice commensuration: the unit length along $<1\bar{1}\bar{2}>$ is 0.9564 nm, which is three times the in-plane S-S distance in MoS_2 (0.316 nm) with a 0.9% difference. Secondly, $[1\bar{1}0]$, $[1\bar{1}\bar{2}]$, and $[1\bar{1}2]$ on $SrTiO_3(110)$ form a set of directions arranged in a nearly-regular-hexagonal way (Figure 4c), with included angles of 70°, 55°, 55°.

In practice, an equilateral triangle of MoS_2 cannot be distorted to a 70°/55°/55° triangle whilst maintaining a perfect crystal structure; this would require an unphysical compressive strain of 18%. Figure 4e is a close-up SEM image of a crystal with its edges outlined in black, with an overall shape of a 70°/55°/55° triangle. Some internal angles are still 60°, which point to a perfect MoS_2 lattice, while some angles are closer to 55°, meaning the lattice may have been partially rotated and/or distorted to align one edge with $<1\bar{1}\bar{2}>$. Figure 4f presents an atomic model of MoS_2 that follows the shape in Figure 4e, including the zig-zags and the notches along the edges with a sulfur termination. The bottom edge of the crystal is parallel to $[1\bar{1}0]$ on the substrate, along 'd_1' labelled, which is a distance corresponding to 7 unit lengths in MoS_2 and 4 unit lengths along $SrTiO_3[1\bar{1}0]$. The MoS_2 crystal also has some parts of its lattice rotated to align one edge with $<1\bar{1}\bar{2}>$ of $SrTiO_3$, highlighted in yellow. 'd_2' is labelled along the $[1\bar{1}2]$ direction, and its length represents 1 unit length along $[1\bar{1}2]$ and 3 unit lengths in MoS_2. The fact that this MoS_2 crystal tries to align with both $<1\bar{1}0>$ and $<1\bar{1}\bar{2}>$ inevitably induces lattice defects (e.g., around the rotated areas) plus a small degree of lattice distortion. The associated strain is confirmed by PL spectroscopy (see later). On $SrTiO_3(110)$, the interfacial crystallographic relationship is '$(0001)_{MoS_2} \parallel (110)_{SrTiO_3}$, $[2\bar{1}\bar{1}0]_{MoS_2} \parallel$

$[1\bar{1}0]_{\mathrm{SrTiO_3}}$', and partially '$(0001)_{\mathrm{MoS_2}} \parallel (110)_{\mathrm{SrTiO_3}}$, $[2\bar{1}\bar{1}0]_{\mathrm{MoS_2}} \parallel [1\bar{1}\bar{2}]_{\mathrm{SrTiO_3}}$'.

3.3. MoS_2 on $SrTiO_3(001)$.

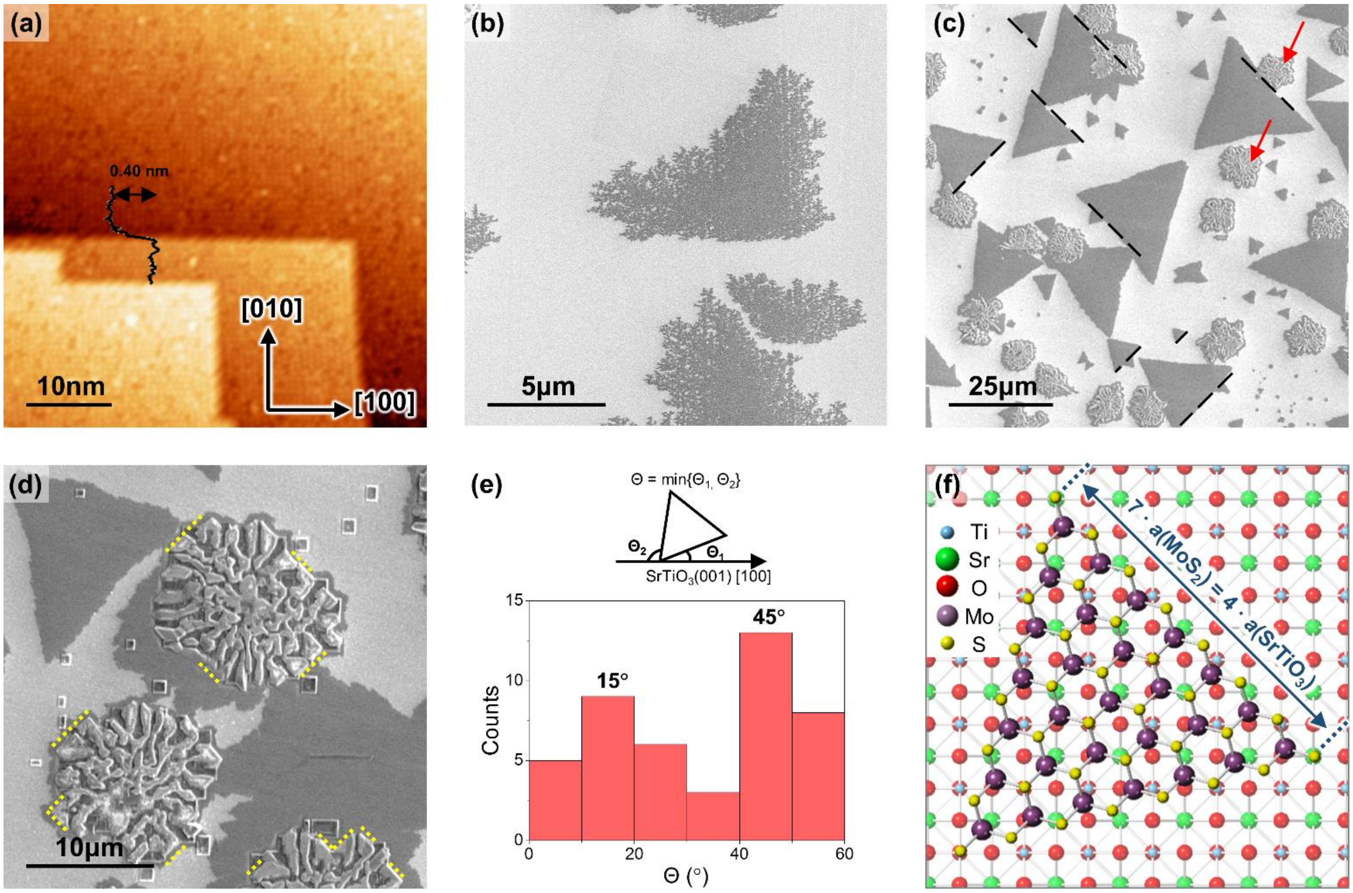

Figure 5. Models and images of $SrTiO_3(001)$ and MoS_2 on $SrTiO_3(001)$. (a) STM image of $SrTiO_3(001)$ showing terraces consisting of the $c(4 \times 2)$ reconstruction. The step height is 0.40 ± 0.04 nm, corresponding to the d_{001} lattice spacing ($V_s = 2.0$ V, $I_t = 0.15$ nA). (b) SEM image of MoS_2 crystals on $SrTiO_3(001)$ with a dendritic morphology. (c) SEM image of MoS_2 crystals on $SrTiO_3(001)$ grown with a shorter source–substrate distance in the CVD furnace. The monolayer crystals are compact and much larger than the dendrites (dark triangles), with few-layer (to bulk) MoS_2 also formed (indicated by red arrows). (d) SEM images of few-layer (to bulk) MoS_2 structures. (e) Orientation

histogram of monolayer MoS_2 crystals, measured according to the standard above. (f) Atomic model of MoS_2 on $SrTiO_3(001)$. 7 MoS_2 unit cell lengths (S-S spacings) = 4 $SrTiO_3[1\bar{1}0]$ unit lengths (Sr-Sr spacings). The substrate lattice directions in (a) also apply to panels (b,c,d,f).

On the final surface in our study, $SrTiO_3(001)$, we generated the $c(4 \times 2)$ reconstruction as shown in Figure 5a.[25,42,43] It was produced by Ar^+ ion sputtering at 500 eV for 10 minutes, followed by annealing at 1100 °C for 30 minutes in UHV.

MoS_2 crystals grown on $SrTiO_3(001)$ clearly show a distinct morphology compared with the other $SrTiO_3$ terminations (Figure 5b). The dendritic growth of MoS_2 on $SrTiO_3(001)$ has been studied by Zhang *et al.*[44,45] and will not be discussed further here. For comparison, during the same CVD growth on an amorphous silica substrate, placed side by side with the $SrTiO_3$ sample, the MoS_2 crystals are perfectly sharp and triangular (Figure 2). Therefore, the dendritic growth can be safely attributed to the substrate effect of $SrTiO_3(001)$.

To consistently study the epitaxy of compact crystals, we obtained compact triangular crystals when we placed the precursors closer to the substrate in the CVD furnace.[44] The resulting crystals are shown in Figure 5c, which are compact and much larger than the dendrites (note the very different scale bars in Figure 5b and c), and no dendrites are observed. Using these growth conditions, it was difficult to completely avoid building up few-layer (to bulk) MoS_2 structures, as indicated by the red arrows. A close-up SEM image of these structures is shown in Figure 5d. The monolayer MoS_2 crystals in Figure 5c (dark triangles) are measured in terms of their crystal orientations, and the resulting histogram is shown in Figure 5e. Two peaks are identified at 15° and 45°, relative to the substrate [100] direction. They are two crystallographically equivalent orientations because of the four-fold symmetry of $SrTiO_3$(001). The interfacial crystallographic relationship can be described as '$(0001)_{MoS_2} \parallel (001)_{SrTiO_3}$, $[2\bar{1}\bar{1}0]_{MoS_2} \parallel [1\bar{1}0]_{SrTiO_3}$'.

Again, in these orientations one edge of the triangular MoS_2 crystal aligns with the $<1\bar{1}0>$ directions on $SrTiO_3$(001) because of the 7:4 coincidence epitaxy. A selection of such edges are highlighted by black dashed lines in Figure 5c. It is also interesting to note that even the few-layer (to bulk) MoS_2 structures have many of their edges aligned with the $<1\bar{1}0>$ directions on $SrTiO_3$(001), as highlighted in yellow in Figure 5d. An atomic model is drawn in Figure 5f to show an example monolayer crystal and the lattice commensuration. It should be noted that the histogram peaks at 15° and 45° are not sharp, because the crystals measured are mostly large (15–30 μm), and their growth is more kinetically controlled than for the smaller ones, as discussed in section 3.1.

3.4. Raman Spectroscopy and PL.

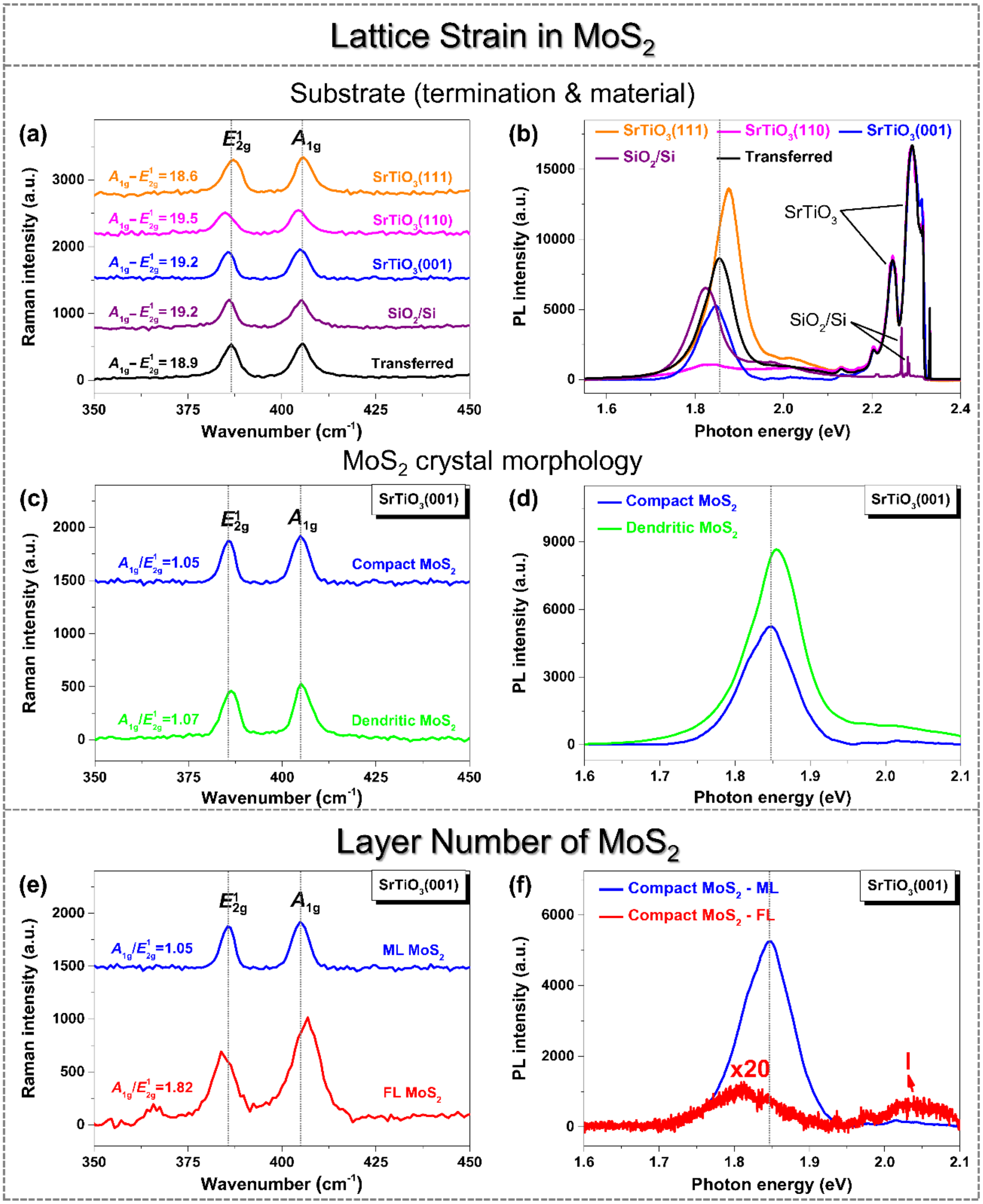

Figure 6. Raman and PL measurements. (a,c,e) Raman and (b,d,f) PL spectra of the MoS_2 single crystals (a,b) on different substrate surfaces, i.e., $SrTiO_3$(111), (110), (001), SiO_2/Si, and the MoS_2 transferred onto $SrTiO_3$, (c,d) with

different morphologies, i.e., compact- and dendritic-shaped MoS_2, and (e,f) with different layer numbers, i.e., monolayer (ML) and few-layer (FL) MoS_2. 'I' indicates the indirect optical transition.

Raman and PL spectroscopy were performed to investigate some of the structural properties of the CVD-grown MoS_2 on different substrates (Figure 6 and 7). The Raman and PL spectra are known to be influenced by the layer thickness,[46] lattice strain,[47–52] doping level,[53,54] and lattice defects[55] of MoS_2. These depend on the substrate surface (Figure 6a,b), the MoS_2 crystal morphology (Figure 6c,d), and the MoS_2 layer number (Figure 6e,f). Detailed information can be extracted through Lorentzian fitting for the PL spectra of monolayer MoS_2 on different substrates (Figure 7). In addition to the samples mentioned previously, we also studied MoS_2 monolayer crystals transferred onto a $SrTiO_3$ substrate. This sample serves as a reference for strain calculations as the crystals have released their strain during the transfer process. Note that the transferred sample is also Nb-doped (0.5 wt%) and was annealed after the transfer to remove the trapped contaminants and improve the MoS_2–$SrTiO_3$ interface adhesion. Therefore its doping level can be considered nearly the same as that in the MoS_2 directly grown on $SrTiO_3$.

Figure 6a,c,e shows the two characteristic Raman modes of MoS_2, $E_{2\mathrm{g}}^1$ (382.0–384.3 cm^{-1}) and $A_{1\mathrm{g}}$ (403.0–407.5 cm^{-1}).[46] The $E_{2\mathrm{g}}^1$ and $A_{1\mathrm{g}}$ modes are preferentially excited for terrace and edge terminations, respectively.[56] Therefore, the relative integrated intensities of $A_{1\mathrm{g}}$ and $E_{2\mathrm{g}}^1$ can provide information on the texture of MoS_2.[26,56,57] Regardless of the substrate, all the MoS_2 monolayers predominant with terrace sites exhibit similar integrated intensity ratios of $A_{1\mathrm{g}}/E_{2\mathrm{g}}^1$ ~1.05, whereas the few-layer MoS_2 terminated more by edges shows an increased ratio of $A_{1\mathrm{g}}/E_{2\mathrm{g}}^1$ ~1.82 (Figure a,c,e), conforming well to those reported previously.[26,46] Also, the frequency difference between $A_{1\mathrm{g}}$ and $E_{2\mathrm{g}}^1$ modes can be used to precisely determine the layer number of MoS_2. Our values are $\leq 19.5\ \mathrm{cm}^{-1}$ for all the monolayer MoS_2 and ≥ 23.1 cm^{-1} for the few-layer MoS_2 (Figure 6a,c,e), in good agreement with the literature.[46] An example of the few-layer structures was shown in Figure 5d. Figure 6f presents the PL of monolayer and few-layer MoS_2 on the same substrate termination, $SrTiO_3(001)$. In addition to the direct transitions (K→K) involving two split valence bands for the emissions of A and B excitons, few-layer MoS_2 shows an additional peak (I) originating from the indirect transition ($\Lambda \rightarrow \Gamma$).[2,3,58] Compared to the monolayer MoS_2, the few-layer MoS_2 exhibits much weaker PL with lower emission energies (monolayer – 1.85 eV for A excitons and 2.02 eV for B excitons; few-layer – 1.81 eV for A excitons, 1.98 eV for B excitons, and 2.04 eV for indirect excitons).

The lattice strain in MoS_2 develops via two processes. The first is epitaxial growth associated with the lattice mismatch between MoS_2 and the substrate. The second is the fast cooling where strain develops due to different thermal expansion coefficients (TEC) of MoS_2 and the substrate.[59] The TEC of the as-prepared 2H-phase MoS_2 ($\alpha_{\mathrm{MoS_2,a}}$ = 1.9 × 10^{-6} K^{-1} and $\alpha_{\mathrm{MoS_2,c}}$ = 8.65 × 10^{-6} K^{-1}, 293–1073 K)[60] is approximately one order of magnitude larger than that of SiO_2 (typical value $\alpha_{\mathrm{SiO_2}}$ = 5.6 × 10^{-7} K^{-1})[61], while it is about one order of magnitude smaller than that of $SrTiO_3$ ($\alpha_{\mathrm{SrTiO_3}}$ = 3.23 × 10^{-5} K^{-1}, 300–1800 K)[62]. As a result, in the fast cooling stage following MoS_2 growth, tensile strain develops in the SiO_2-supported MoS_2 whereas compressive strain is introduced in MoS_2 on $SrTiO_3$.[59] The tensile and compressive strains respectively lead to red and blue shifts of the E_{2g}^{1} and A_{1g} Raman peaks and the A-exciton PL peak, relative to the transferred sample (Figure 6a,b).[47–52] However, these three peaks are all red-shifted for the monolayer MoS_2 crystals grown on $SrTiO_3(110)$ and (001), which is attributed to epitaxial growth. As manifested in Figure 4 and 5, the MoS_2 monolayer crystals show large lattice mismatch with the $SrTiO_3(110)$ and (001) terminations, leading to the tensile strain. To estimate the growth-induced tensile strains in the MoS_2 monolayers grown on $SrTiO_3$(110) and (001), we use their peak shifts of the E_{2g}^1 Raman mode with respect to that on $SrTiO_3$(111).[63] As stated in section 3.1, the small difference of < 0.2% in the lattice parameters between MoS_2 and $SrTiO_3$(111) should give rise to a compressive strain of ~0.18% in the MoS_2 adlayer. Taking this into account, the growth-induced tensile strain is ~0.58% on $SrTiO_3$(110), caused by the attempt of MoS_2 crystal edges to align with both $<1\bar{1}0>$ and $<1\bar{1}\bar{2}>$ crystallographic directions. It is ~0.34% on $SrTiO_3$(001), ascribed to the lattice mismatch along the two non-epitaxial edges of the monolayer MoS_2 crystal. Finally, the growth-induced strain can be considered negligible in the monolayer MoS_2 grown on SiO_2/Si owing to the amorphous substrate surface, which leads to the random orientation of MoS_2 crystals in Figure 2.

Figure 6b also shows that the tensile strains in the monolayer MoS_2 supported on $SrTiO_3$(110), (001), and SiO_2/Si substrates commonly lead to decreased PL intensities compared to the transferred sample.[50] In particular, significant PL quenching is observed on $SrTiO_3$(110), which stems from the epitaxy-induced lattice defects in the crystals previously shown in Figure 4f, which will be discussed later. However, on $SrTiO_3$(111), the PL intensity is enhanced by 58% with a slightly narrower peak width (decrease in the full-width at half-maximum ΔFWHM = 7.05 meV) compared to the transferred sample, due to the compressive strain,[49] which agrees with the Raman results.

Moreover, the crystal morphology also impacts the strain level in MoS_2. As shown in Figure 6c,d, the dendritic MoS_2 crystals on $SrTiO_3$(001) display small blue shifts of Raman peaks and the A-exciton PL peak relative to the compact triangular crystals. (Note that the E_{2g}^1 Raman mode corresponding to the in-plane Mo−S phonon is more sensitive to strain than the A_{1g} mode corresponding to out-of-plane Mo−S phonon.[48–52]) This is because the dendrites could have partially released the growth-induced tensile strain by generating numerous fragmental edges. This suppresses the deterioration of the MoS_2 lattice and its optical properties, which also results in the stronger PL intensity for the dendrites.

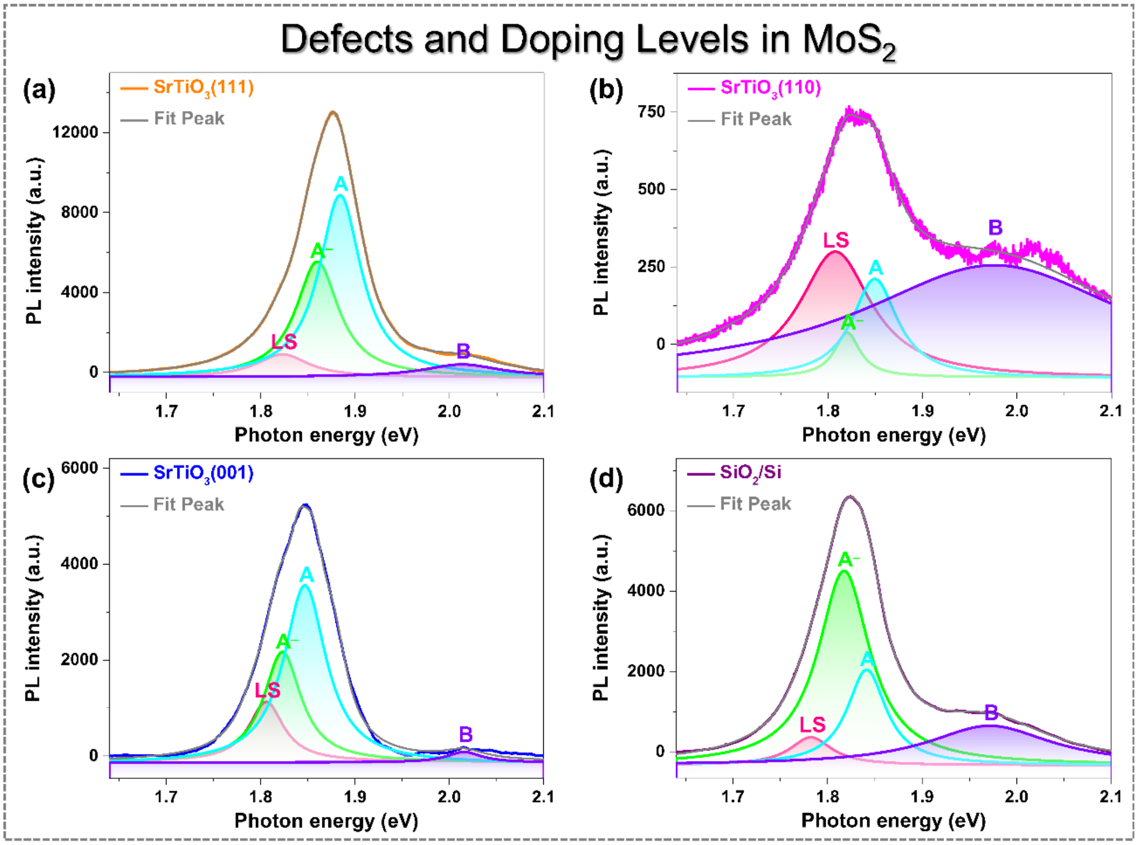

Figure 7. Lorentzian fitted PL spectra of the monolayer MoS_2 grown on (a) $SrTiO_3(111)$, (b) $SrTiO_3(110)$, (c) $SrTiO_3(001)$, and (d) SiO_2/Si substrates, revealing the presence of A excitons (A), B excitons (B), negatively charged A excitons (trions, A^-), and localized states (LS).

The PL spectra are also fitted with the A and A^- peaks for A-exciton emission, the B peak for B-exciton emission, and localized states (LS) correlated with the structural disorder of MoS_2 (Figure 7).[55] The LS peaks indicate the defect level in the as-grown MoS_2 crystals: $SrTiO_3(110) > SrTiO_3(001) > SrTiO_3(111)$. This depends on the degree of lattice mismatch between MoS_2 and the $SrTiO_3$ surface termination. In addition to the neutral A exciton, the negatively charged exciton (trion, A^-) in Figure 7 suggests n-type doping in the monolayer MoS_2 on all substrates. The intensity ratio of exciton to trion peaks (A/A^-) can be used to indicate the doping level.[64] The larger A/A^- ratio on the SiO_2/Si substrate proves that the charge impurities induce heavier n-doping into the supported MoS_2 than the Nb in $SrTiO_3$ substrates. Nonetheless, the doping level of MoS_2 on all $SrTiO_3$ substrates (all Nb-doped at 0.5 wt%) is the same. Therefore, the growth-induced strains can be safely deduced from the Raman and the A-exciton PL peak positions of MoS_2 on different terminations of $SrTiO_3$.

4. DISCUSSION

We have shown that on three different crystal terminations of $SrTiO_3$, MoS_2 crystals tend to adopt the orientations that allow its lattice to match that of the substrate via coincidence epitaxy. The equilibrium orientations and crystal shapes maximize the number of directions along which this is achieved. The interfacial vdW bonding is strengthened in the epitaxial orientations via lattice registry, giving rise to a greater number of bonding sites and closer proximity between the two layers. Therefore, when a MoS_2 nucleus is free to rotate in the initial stage, it gets 'locked' into the lowest-energy orientation,[8] i.e., in the epitaxial configurations we observed. Other bonding types, e.g., electrostatic attraction[7] and chemical bonds,[65] are less likely to exist between MoS_2 and $SrTiO_3$. This is because they are stronger than vdW bonding by orders of magnitude and would lock the MoS_2 monolayers exclusively into certain orientations, e.g., as observed on Au(111).[35] Gold, an electronegative metal, is a very different substrate to $SrTiO_3$, an oxide ceramic, and can interact with MoS_2 via a stronger bonding type. The Nb doping (0.5 wt%) which makes $SrTiO_3$ conductive may also have played a role in its bonding with MoS_2 monolayers, but we expect any effects to be minimal.

On $SrTiO_3$(111), it is advantageous to align the $<2\bar{1}\bar{1}0>$ directions of MoS_2 with $<1\bar{1}0>$ on $SrTiO_3$ with favorable coincidence lattice registry. In previous studies of MoS_2 grown on ceramic substrates, SiO_2 does not induce epitaxy as it is amorphous;[12] *c*-plane sapphire, another three-fold symmetric substrate, reveals similar preferred orientations to MoS_2 on $SrTiO_3$(111) (0° and 60°).[7,8] In these orientations, either interfacial electrostatic attraction (as a result of charge transfer)[7] or greatly enhanced vdW bonding[8] were proposed. It was not explicitly mentioned why the interfacial bonding prefers particular orientations, but this is likely to be the good lattice registry between MoS_2 and sapphire. Their in-plane periodicities, 0.316 nm for MoS_2 and 0.476 nm for sapphire, have a 2:3 ratio with a 0.4% difference.[7] Therefore we speculate that both $SrTiO_3$(111) and *c*-plane sapphire show similar low-energy coincidence epitaxial relationships because of lattice commensuration with negligible strain.

Also, one of the two lattice-coincident orientations on $SrTiO_3$(111) is more strongly preferred, and a similar situation is found in the MoS_2-on-Au(111) system. A single Au(111) layer is six-fold symmetric, while a second layer reduces it to three-fold because of the differentiated fcc and hcp sites. Theoretical studies by Bruix *et al.* reveal a very slim energy difference (16 meV per unit cell) between the 'MoS_2-on-hcp' and 'MoS_2-on-fcc' configurations,[17] but the crystals turn out to exclusively orient in only one way.[35] The termination of Au(111) alternates between hcp and fcc across a ridge of the herringbone structure, so that the MoS_2 triangles 'flipping' their directions across each ridge means the same stacking. This exclusivity is also assisted by a much slower growth method adopted than CVD, which results in nanometer-sized crystals (all < 8 nm).[35] On the other hand, $SrTiO_3$(111) shows a uniform termination with surface step heights always equivalent to the d_{111} lattice parameter.[23,66] Hence, the 0° and 60° orientations of MoS_2 are indeed distinct, possibly with a very small but noticeable energy difference like on Au(111).

On $SrTiO_3$(110), the strong tendency to maximize coincidence epitaxial directions (i.e., $<1\bar{1}0>$ and $<1\bar{1}\bar{2}>$) competes with the equilibrium shape of MoS_2 crystals. To accommodate the shape distortions, there is an increased defect density and an additional element of strain energy. These both increase the lattice energy of MoS_2 but must have been overcome by the reduction in the interfacial energy because of the improved bonding. Even on $SrTiO_3$(001), where it is only possible to satisfy one direction of good coincidence epitaxy along $<1\bar{1}0>$, the MoS_2 crystals still show a preference to orient in such a way.

It is worth noting that as the substrate surface reconstructions prepared in vacuum do not usually survive in atmosphere, we do not know what the exact interface is at the time of CVD growth of MoS_2. It cannot be the bulk termination of $SrTiO_3$ because the surface bonds tend to rearrange themselves to stabilize surface polarity. However, we do know that there are certain ways in which $SrTiO_3$ reconstructs. For example, $SrTiO_3$(111)-(4 × 4) is one of the lowest-energy reconstruction of the (111) termination, which forms most easily in partial pressures of oxygen.[23,34] If MoS_2 grows on $SrTiO_3$(111)-(4 × 4), the substrate periodicity (i.e., the unit length along $<1\bar{1}0>$) becomes four times that of the bulk. The coincidence epitaxy then turns into a 7:1 ratio, which is an attractive epitaxial relationship. On $SrTiO_3$(110), (1 × 4), (3 × 4), (4 × 4), and (6 × 4) reconstructions have been reported previously,[24,67] which make the periodicity along $<1\bar{1}0>$ four times that in the bulk as well. Similarly on $SrTiO_3$(001), there is the (4 × 4) reconstruction which does the same thing; there is also a *c*(4 × 4) reconstruction, which makes the periodicity along $<1\bar{1}0>$ $2\sqrt{2}$ times that of the bulk, and this turns the coincidence epitaxy into a 5:1 ratio with a mismatch of 1.2%.

Based on the above, our understanding of what drives the epitaxy is the interfacial lattice commensuration between $<2\bar{1}\bar{1}0>$ (i.e., the sulfur edge directions) of MoS_2 and $<1\bar{1}0>$ on $SrTiO_3$. We would like to stress the strength of this vdW interaction that can powerfully control the growth of MoS_2 crystals. Developing a deeper understanding of MoS_2 epitaxy is an important step towards integrating MoS_2 in future novel electronic devices. This is because when MoS_2 is grown in perfect lattice registry with its crystalline substrate, grain boundaries are eliminated. This allows large-area monolayers of MoS_2 to be grown even when there are multiple nucleation sites.

Finally, we would like to mention that it is very difficult to obtain atomically resolved STM images of MoS_2 on a ceramic substrate and a high-resolution image like Figure 3e is rare. If such images could be obtained on all terminations of $SrTiO_3$ substrates, they would provide useful information about the strain or lattice distortion in monolayer MoS_2. Many good atomic images of MoS_2 monolayers on Au(111) have been reported,[15,17,35,36,39] but it was difficult for the same group of researchers to obtain high resolution images of MoS_2 on TiO_2.[65] It is not yet clear to us why it is a lot harder to image MoS_2 on ceramic substrates than on metal substrates. This is no doubt an interesting area for future study.

5. CONCLUSIONS

In summary, the orientations and shapes of MoS_2 crystals are strongly influenced by substrate interactions with $SrTiO_3$. The equilibrium orientations maximize the interfacial vdW bonding via coincidence epitaxy and hence enhanced bonding, which is assisted by lattice defects and crystal shape distortions when possible. This offers a broader interpretation of epitaxy, which involves minimizing the total energy of the system in a more complex way. It is the sum of the lattice energy of MoS_2 (to maintain its equilateral triangular shape) and the interfacial energy associated with the MoS_2–substrate interactions. The results also confirm that the vdW interaction is sufficiently strong to regulate epitaxy in a powerful way. The strain levels in MoS_2 are found to be adjusted by the different epitaxial relations with the substrate. This allows us more rigorous control in the synthesis of large-scale uniform MoS_2 layers for optimal electronic properties and enables the manipulation of inbuilt strains to fine tune the bandgap, which improve the applicability of monolayer MoS_2 in next-generation nanoelectronic devices such as transistors.

■ AUTHOR INFORMATION

Corresponding Authors

*Email: martin.castell@materials.ox.ac.uk. (M.R.C.)

*Email: peiyu.chen@materials.ox.ac.uk. (P.C.)

Author Contributions

[†]P.C. and W.X. contributed equally.

Notes

The authors declare no competing financial interest.

■ ACKNOWLEDGMENTS

The authors would like to thank Chris Spencer (JEOL UK) for technical support and Dr. Krishnan Murugappan and Jiawei Jiang for taking SEM images on the Zeiss Merlin. We are also grateful to the EPSRC for funding, Grant No.: EP/K032518/1. J.H.W. is supported by the Royal Society and the European Research Council, Grant No.: 725258 LATO CoG 2016.

■ REFERENCES

(1) Ryder, C. R.; Wood, J. D.; Wells, S. A.; Hersam, M. C. Chemically Tailoring Semiconducting Two-Dimensional Transition Metal Dichalcogenides and Black Phosphorus. *ACS Nano* **2016**, *10*, 3900−3917.

(2) Mak, K. F.; Lee, C.; Hone, J.; Shan, J.; Heinz, T. F. Atomically Thin MoS_2: A New Direct-Gap Semiconductor. *Phys. Rev. Lett.* **2010**, *105*, 136805.

(3) Splendiani, A.; Sun, L.; Zhang, Y.; Li, T.; Kim, J.; Chim, C. Y.; Galli, G.; Wang, F. Emerging Photoluminescence in Monolayer MoS_2. *Nano Lett.* **2010**, *10*, 1271–1275.

(4) Li, H.; Wu, J.; Yin, Z.; Zhang, H. Preparation and Applications of Mechanically Exfoliated Single-Layer and Multilayer MoS_2 and WSe_2 Nanosheets. *Acc. Chem. Res.* **2014**, *47*, 1067–1075.

(5) Radisavljevic, B.; Radenovic, A.; Brivio, J.; Giacometti, V.; Kis, A. Single-Layer MoS_2 Transistors. *Nat. Nanotechnol.* **2011**, *6*, 147–150.

(6) Lee, Y. H.; Zhang, X. Q.; Zhang, W.; Chang, M. T.; Lin, C. Te; Chang, K. Di; Yu, Y. C.; Wang, J. T. W.; Chang, C. S.; Li, L. J.; Lin, T. W. Synthesis of Large-Area MoS_2 Atomic Layers with Chemical Vapor Deposition. *Adv. Mater.* **2012**, *24*, 2320–2325.

(7) Ji, Q.; Kan, M.; Zhang, Y.; Guo, Y.; Shi, J.; Sun, Q.; Chen, Q.; Zhang, Y.; Liu, Z. Unravelling Orientation Distribution and Merging Behavior of Monolayer MoS_2 Domains on Sapphire. *Nano Lett.* **2015**, *15*, 198–205.

(8) Dumcenco, D.; Ovchinnikov, D.; Marinov, K.; Lazić, P.; Gibertini, M.; Marzari, N.; Sanchez, O.

L.; Kung, Y. C.; Krasnozhon, D.; Chen, M. W.; Bertolazzi, S.; Gillet, P.; Fontcuberta i Morral, A.; Radenovic, A.; Kis, A. Large-Area Epitaxial Monolayer MoS_2. *ACS Nano* **2015**, *9*, 4611–4620.

(9) Najmaei, S.; Amani, M.; Chin, M. L.; Liu, Z.; Birdwell, A. G.; O'Regan, T. P.; Ajayan, P. M.; Dubey, M.; Lou, J. Electrical Transport Properties of Polycrystalline Monolayer Molybdenum Disulfide. *ACS Nano* **2014**, *8*, 7930–7937.

(10) Zhang, J.; Yu, H.; Chen, W.; Tian, X.; Liu, D.; Cheng, M.; Xie, G.; Yang, W.; Yang, R.; Bai, X.; Shi, D.; Zhang, G. Scalable Growth of High-Quality Polycrystalline MoS_2 Monolayers on SiO_2 with Tunable Grain Sizes. *ACS Nano* **2014**, *8*, 6024–6030.

(11) van der Zande, A. M.; Huang, P. Y.; Chenet, D. A.; Berkelbach, T. C.; You, Y.; Lee, G. H.; Heinz, T. F.; Reichman, D. R.; Muller, D. A.; Hone, J. C. Grains and Grain Boundaries in Highly Crystalline Monolayer Molybdenum Disulphide. *Nat. Mater.* **2013**, *12*, 554–561.

(12) Wang, S.; Rong, Y.; Fan, Y.; Pacios, M.; Bhaskaran, H.; He, K.; Warner, J. H. Shape Evolution of Monolayer MoS_2 Crystals Grown by Chemical Vapor Deposition. *Chem. Mater.* **2014**, *26*, 6371–6379.

(13) Ago, H.; Endo, H.; Solís-Fernández, P.; Takizawa, R.; Ohta, Y.; Fujita, Y.; Yamamoto, K.; Tsuji, M. Controlled van Der Waals Epitaxy of Monolayer MoS_2 Triangular Domains on Graphene. *ACS Appl. Mater. Interfaces* **2015**, *7*, 5265–5273.

(14) Liu, T.; Temprano, I.; King, D. A.; Driver, S. M.; Jenkins, S. J. Epitaxial Growth of Few-Layer $MoS_2(0001)$ on $FeS_2\{100\}$. *Chem. Commun.* **2015**, *51*, 537–540.

(15) Sørensen, S. G.; Füchtbauer, H. G.; Tuxen, A. K.; Walton, A. S.; Lauritsen, J. V. Structure and Electronic Properties of In Situ Synthesized Single-Layer MoS_2 on a Gold Surface. *ACS Nano* **2014**, *8*, 6788–6796.

(16) Liu, K.; Zhang, L.; Cao, T.; Jin, C.; Qiu, D.; Zhou, Q.; Zettl, A.; Yang, P.; Louie, S. G.; Wang, F. Evolution of Interlayer Coupling in Twisted Molybdenum Disulfide Bilayers. *Nat. Commun.* **2014**, *5*, 4966.

(17) Bruix, A.; Miwa, J. A.; Hauptmann, N.; Wegner, D.; Ulstrup, S.; Grønborg, S. S.; Sanders, C. E.; Dendzik, M.; Grubišić Čabo, A.; Bianchi, M.; Lauritsen, J. V.; Khajetoorians, A. A.; Hammer, B.; Hofmann, P. Single-Layer MoS_2 on Au(111): Band Gap Renormalization and Substrate Interaction. *Phys. Rev. B* **2016**, *93*, 165422.

(18) Farmanbar, M.; Brocks, G. First-Principles Study of van Der Waals Interactions and Lattice Mismatch at MoS_2/Metal Interfaces. *Phys. Rev. B* **2016**, *93*, 085304.

(19) Chen, W.; Santos, E. J. G.; Zhu, W.; Kaxiras, E.; Zhang, Z. Tuning the Electronic and Chemical Properties of Monolayer MoS_2 Adsorbed on Transition Metal Substrates. *Nano Lett.* **2013**, *13*, 509–514.

(20) Yun, W. S.; Lee, J. D. Schottky Barrier Tuning of the Single-Layer MoS_2 on Magnetic Metal Substrates Through Vacancy Defects and Hydrogenation. *Phys. Chem. Chem. Phys.* **2016**, *18*, 31027–31032.

(21) Naito, M.; Sato, H. Reflection High-Energy Electron Diffraction Study on the $SrTiO_3$ Surface

Structure. *Phys. C Supercond.* **1994**, *229*, 1–11.

(22) Noland, J. A. Optical Absorption of Single-Crystal Strontium Titanate. *Phys. Rev.* **1954**, *94*, 724–724.

(23) Russell, B. C.; Castell, M. R. Surface of Sputtered and Annealed Polar $SrTiO_3(111)$: TiO_x-Rich (n × n) Reconstructions. *J. Phys. Chem. C* **2008**, *112*, 6538–6545.

(24) Russell, B. C.; Castell, M. R. Reconstructions on the Polar $SrTiO_3(110)$ Surface: Analysis Using STM, LEED, and AES. *Phys. Rev. B* **2008**, *77*, 245414.

(25) Castell, M. R. Scanning Tunneling Microscopy of Reconstructions on the $SrTiO_3(001)$ Surface. *Surf. Sci.* **2002**, *505*, 1–13.

(26) Xu, W.; Li, S.; Zhou, S.; Lee, J. K.; Wang, S.; Sarwat, S. G.; Wang, X.; Bhaskaran, H.; Pasta, M.; Warner, J. H. Large Dendritic Monolayer MoS_2 Grown by Atmospheric Pressure Chemical Vapor Deposition for Electrocatalysis. *ACS Appl. Mater. Interfaces* **2018**, *10*, 4630–4639.

(27) Jones, L.; Yang, H.; Pennycook, T. J.; Marshall, M. S. J.; Van Aert, S.; Browning, N. D.; Castell, M. R.; Nellist, P. D. Smart Align—A New Tool for Robust Non-Rigid Registration of Scanning Microscope Data. *Adv. Struct. Chem. Imaging* **2015**, *1*, 8.

(28) Jones, L.; Wang, S.; Hu, X.; ur Rahman, S.; Castell, M. R. Maximising the Resolving Power of the Scanning Tunneling Microscope. *Adv. Struct. Chem. Imaging* **2018**, *4*, 7.

(29) Horcas, I.; Fernández, R.; Gómez-Rodríguez, J. M.; Colchero, J.; Gómez-Herrero, J.; Baro, A. M. WSXM: A Software for Scanning Probe Microscopy and a Tool for Nanotechnology. *Rev. Sci.*

Instrum. **2007**, *78*, 013705.

(30) Fu, Y.; Feng, X.; Yan, M. F.; Wang, K.; Wang, S. First Principle Study on Electronic Structure and Optical Phonon Properties of 2H-MoS_2. *Phys. B Condens. Matter* **2013**, *426*, 103–107.

(31) Moffatt, W. G.; Pearsall, G. W.; Wulff, J. *Structure and Properties of Materials (Volume 1: Structure)*; John Wiley & Sons Inc., 1964.

(32) Niewczas, M. Lattice Correspondence During Twinning in Hexagonal Close-Packed Crystals. *Acta Mater.* **2010**, *58*, 5848–5857.

(33) Dai, Z.; Jin, W.; Grady, M.; Sadowski, J. T.; Dadap, J. I.; Osgood, R. M.; Pohl, K. Surface Structure of Bulk 2H-MoS_2(0001) and Exfoliated Suspended Monolayer MoS_2: A Selected Area Low Energy Electron Diffraction Study. *Surf. Sci.* **2017**, *660*, 16–21.

(34) Marks, L. D.; Chiaramonti, A. N.; Rahman, S. U.; Castell, M. R. Transition from Order to Configurational Disorder for Surface Reconstructions on $SrTiO_3$(111). *Phys. Rev. Lett.* **2015**, *114*, 226101.

(35) Helveg, S.; Lauritsen, J. V.; Lægsgaardd, E.; Stensgaard, I.; Nørskov, J. K.; Clausen, B. S.; Topsøe, H.; Besenbacher, F. Atomic-Scale Structure of Single-Layer MoS_2 Nanoclusters. *Phys. Rev. Lett.* **2000**, *84*, 951–954.

(36) Lauritsen, J. V.; Kibsgaard, J.; Topsøe, H.; Helveg, S.; Clausen, B. S.; Lægsgaard, E.; Besenbacher, F. Size-Dependent Structure of MoS_2 Nanocrystals. *Nat. Nanotechnol.* **2007**, *2*, 53–58.

(37) Jiang, C.; Rumyantsev, S. L.; Samnakay, R.; Shur, M. S.; Balandin, A. A. High-Temperature Performance of MoS_2 Thin-Film Transistors: Direct Current and Pulse Current-Voltage Characteristics. *J. Appl. Phys.* **2015**, *117*, 064301.

(38) Magonov, S. N.; Whangbo, M. H. Interpreting STM and AFM Images. *Adv. Mater.* **1994**, *6*, 355–371.

(39) Grønborg, S. S.; Ulstrup, S.; Bianchi, M.; Dendzik, M.; Sanders, C. E.; Lauritsen, J. V.; Hofmann, P.; Miwa, J. A. Synthesis of Epitaxial Single-Layer MoS_2 on Au(111). *Langmuir* **2015**, *31*, 9700–9706.

(40) Enterkin, J. A.; Subramanian, A. K.; Russell, B. C.; Castell, M. R.; Poeppelmeier, K. R.; Marks, L. D. A Homologous Series of Structures on the Surface of $SrTiO_3$(110). *Nat. Mater.* **2010**, *9*, 245–248.

(41) Wang, Z.; Loon, A.; Subramanian, A.; Gerhold, S.; Mcdermott, E.; Enterkin, J. A.; Hieckel, M.; Russell, B. C.; Green, R. J.; Moewes, A.; Guo, J.; Blaha, P; Castell, M. R.; Diebold, U.; Marks, L. D. Transition from Reconstruction toward Thin Film on the (110) Surface of Strontium Titanate. *Nano Lett.* **2016**, *16*, 2407−2412.

(42) Becerra-Toledo, A. E.; Marshall, M. S. J.; Castell, M. R.; Marks, L. D. c(4 × 2) and Related Structural Units on the $SrTiO_3$(001) Surface: Scanning Tunneling Microscopy, Density Functional Theory, and Atomic Structure. *J. Chem. Phys.* **2012**, *136*, 214701.

(43) Erdman, N.; Warschkow, O.; Asta, M.; Poeppelmeier, K. R.; Ellis, D. E.; Marks, L. D. Surface

Structures of $SrTiO_3$ (001): A TiO_2-Rich Reconstruction with a c(4 × 2) Unit Cell. *J. Am. Chem. Soc.* **2003**, *125*, 10050–10056.

(44) Zhang, Y.; Ji, Q.; Han, G. F.; Ju, J.; Shi, J.; Ma, D.; Sun, J.; Zhang, Y.; Li, M.; Lang, X. Y.; Zhang, Y.; Liu, Z. Dendritic, Transferable, Strictly Monolayer MoS_2 Flakes Synthesized on $SrTiO_3$ Single Crystals for Efficient Electrocatalytic Applications. *ACS Nano* **2014**, *8*, 8617–8624.

(45) Zhang, Y.; Ji, Q.; Wen, J.; Li, J.; Li, C.; Shi, J.; Zhou, X.; Shi, K.; Chen, H.; Li, Y.; Deng, S.; Xu, N.; Liu, Z.; Zhang, Y. Monolayer MoS_2 Dendrites on a Symmetry-Disparate $SrTiO_3$ (001) Substrate: Formation Mechanism and Interface Interaction. *Adv. Funct. Mater.* **2016**, *26*, 3299–3305.

(46) Lee, C.; Yan, H.; Brus, L. E.; Heinz, T. F.; Hone, J.; Ryu, S. Anomalous Lattice Vibrations of Single- and Few-Layer MoS_2. *ACS Nano* **2010**, *4*, 2695–2700.

(47) He, K.; Poole, C.; Mak, K. F.; Shan, J. Experimental Demonstration of Continuous Electronic Structure Tuning via Strain in Atomically Thin MoS_2. *Nano Lett.* **2013**, *13*, 2931–2936.

(48) Rice, C.; Young, R. J.; Zan, R.; Bangert, U.; Wolverson, D.; Georgiou, T.; Jalil, R.; Novoselov, K. S. Raman-Scattering Measurements and First-Principles Calculations of Strain-Induced Phonon Shifts in Monolayer MoS_2. *Phys. Rev. B* **2013**, *87*, 081307.

(49) Hui, Y. Y.; Liu, X.; Jie, W.; Chan, N. Y.; Hao, J.; Hsu, Y. T.; Li, L. J.; Guo, W.; Lau, S. P. Exceptional Tunability of Band Energy in a Compressively Strained Trilayer MoS_2 Sheet. *ACS Nano* **2013**, *7*, 7126–7131.

(50) Conley, H. J.; Wang, B.; Ziegler, J. I.; Haglund, R. F.; Pantelides, S. T.; Bolotin, K. I. Bandgap Engineering of Strained Monolayer and Bilayer MoS_2. *Nano Lett.* **2013**, *13*, 3626–3630.

(51) Wang, Y.; Cong, C.; Qiu, C.; Yu, T. Raman Spectroscopy Study of Lattice Vibration and Crystallographic Orientation of Monolayer MoS_2 Under Uniaxial Strain. *Small* **2013**, *9*, 2857–2861.

(52) Scalise, E.; Houssa, M.; Pourtois, G.; Afanas′ev, V. V.; Stesmans, A. First-Principles Study of Strained 2D MoS_2. *Phys. E Low-Dimensional Syst. Nanostructures* **2014**, *56*, 416–421.

(53) Azcatl, A.; Qin, X.; Prakash, A.; Zhang, C.; Cheng, L.; Wang, Q.; Lu, N.; Kim, M. J.; Kim, J.; Cho, K.; Addou, R.; Hinkle, C. L.; Appenzeller, J.; Wallace, R. M. Covalent Nitrogen Doping and Compressive Strain in MoS_2 by Remote N_2 Plasma Exposure. *Nano Lett.* **2016**, *16*, 5437–5443.

(54) Nipane, A.; Karmakar, D.; Kaushik, N.; Karande, S.; Lodha, S. Few-Layer MoS_2 p-Type Devices Enabled by Selective Doping Using Low Energy Phosphorus Implantation. *ACS Nano* **2016**, *10*, 2128–2137.

(55) Qiu, H.; Xu, T.; Wang, Z.; Ren, W.; Nan, H.; Ni, Z.; Chen, Q.; Yuan, S.; Miao, F.; Song, F.; Long, G.; Shi, Y.; Sun, L.; Wang, J.; Wang, X. Hopping Transport Through Defect-Induced Localized States in Molybdenum Disulphide. *Nat. Commun.* **2013**, *4*, 2642.

(56) Kong, D.; Wang, H.; Cha, J. J.; Pasta, M.; Koski, K. J.; Yao, J.; Cui, Y. Synthesis of MoS_2 and $MoSe_2$ Films with Vertically Aligned Layers. *Nano Lett.* **2013**, *13*, 1341–1347.

(57) Li, S.; Wang, S.; Salamone, M. M.; Robertson, A. W.; Nayak, S.; Kim, H.; Tsang, S. C. E.; Pasta,

M.; Warner, J. H. Edge-Enriched 2D MoS_2 Thin Films Grown by Chemical Vapor Deposition for Enhanced Catalytic Performance. *ACS Catal.* **2017**, *7*, 877–886.

(58) Zhao, W.; Ribeiro, R. M.; Toh, M.; Carvalho, A.; Kloc, C.; Castro Neto, A. H.; Eda, G. Origin of Indirect Optical Transitions in Few-Layer MoS_2, WS_2, and WSe_2. *Nano Lett.* **2013**, *13*, 5627–5634.

(59) Liu, Z.; Amani, M.; Najmaei, S.; Xu, Q.; Zou, X.; Zhou, W.; Yu, T.; Qiu, C.; Birdwell, A. G.; Crowne, F. J.; Vajtai, R.; Yakobson, B. I.; Xia, Z.; Dubey, M.; Ajayan, P. M.; Lou, J. Strain and Structure Heterogeneity in MoS_2 Atomic Layers Grown by Chemical Vapour Deposition. *Nat. Commun.* **2014**, *5*, 5246.

(60) El-Mahalawy, S. H.; Evans, B. L. The Thermal Expansion of 2H-MoS_2, 2H-$MoSe_2$ and 2H-WSe_2 between 20 and 800 °C. *J. Appl. Crystallogr.* **1976**, *9*, 403–406.

(61) El-Kareh, B. *Fundamentals of Semiconductor Processing Technology*; Springer, 1995.

(62) de Ligny, D.; Richet, P. High-Temperature Heat Capacity and Thermal Expansion of $SrTiO_3$ and $SrZrO_3$ Perovskites. *Phys. Rev. B* **1996**, *53*, 3013–3022.

(63) Castellanos-Gomez, A.; Roldán, R.; Cappelluti, E.; Buscema, M.; Guinea, F.; Van Der Zant, H. S. J.; Steele, G. A. Local Strain Engineering in Atomically Thin MoS_2. *Nano Lett.* **2013**, *13*, 5361–5366.

(64) Wang, S.; Wang, X.; Warner, J. H. All Chemical Vapor Deposition Growth of MoS_2: H-BN Vertical van Der Waals Heterostructures. *ACS Nano* **2015**, *9*, 5246–5254.

(65) Kibsgaard, J.; Clausen, B. S.; Topsøe, H.; Lægsgaard, E.; Lauritsen, J. V.; Besenbacher, F.

Scanning Tunneling Microscopy Studies of TiO_2-Supported Hydrotreating Catalysts: Anisotropic Particle Shapes by Edge-Specific MoS_2–Support Bonding. *J. Catal.* **2009**, *263*, 98–103.

(66) Russell, B. C.; Castell, M. R. $(\sqrt{13} \times \sqrt{13})R13.9^\circ$ and $(\sqrt{7} \times \sqrt{7})R19.1^\circ$ Reconstructions of the Polar $SrTiO_3$(111) Surface. *Phys. Rev. B* **2007**, *75*, 155433.

(67) Brunen, J.; Zegenhagen, J. Investigation of the $SrTiO_3$(110) Surface by Means of LEED, Scanning Tunneling Microscopy and Auger Spectroscopy. *Surf. Sci.* **1997**, *389*, 349–365.

ABSTRACT GRAPHIC